# Contact resonance atomic force microscopy imaging in air and water using photothermal excitation

Marta Kocun, Aleksander Labuda, Anil Gannepalli, and Roger Proksch

## Articles you may be interested in

Nanomechanical imaging of soft samples in liquid using atomic force microscopy
J. Appl. Phys. **114**, 134313 (2013); 10.1063/1.4824080

Dual resonance excitation system for the contact mode of atomic force microscopy
Rev. Sci. Instrum. **83**, 043703 (2012); 10.1063/1.3702799

Phase image contrast mechanism in intermittent contact atomic force microscopy
J. Appl. Phys. **108**, 094311 (2010); 10.1063/1.3503478

In vivo nanomechanical imaging of blood-vessel tissues directly in living mammals using atomic force microscopy
Appl. Phys. Lett. **95**, 013704 (2009); 10.1063/1.3167546

Torsional resonance atomic force microscopy in water
Appl. Phys. Lett. **92**, 053103 (2008); 10.1063/1.2841701
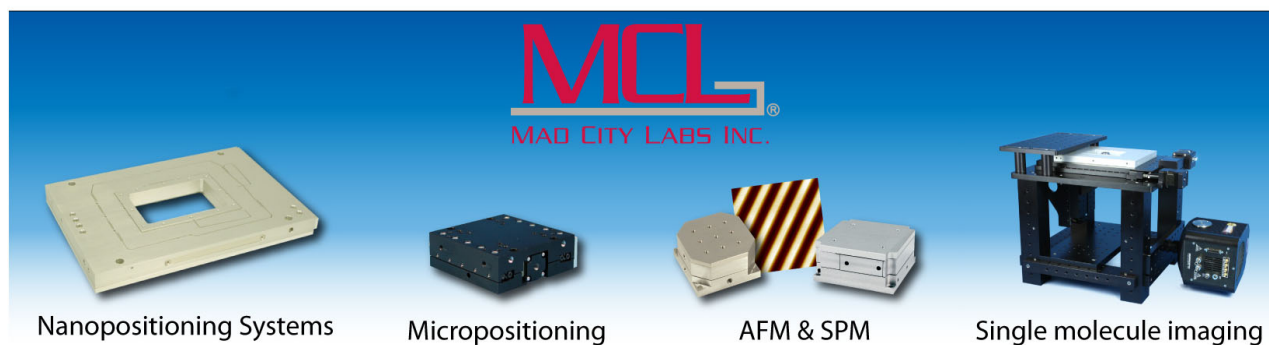
# Contact resonance atomic force microscopy imaging in air and water using photothermal excitation

Marta Kocun, Aleksander Labuda, Anil Gannepalli, and Roger Proksch[a)]
*Asylum Research, an Oxford Instruments Company, Santa Barbara, California 93117, USA*

Contact Resonance Force Microscopy (CR-FM) is a leading atomic force microscopy technique for measuring viscoelastic nano-mechanical properties. Conventional piezo-excited CR-FM measurements have been limited to imaging in air, since the "forest of peaks" frequency response associated with acoustic excitation methods effectively masks the true cantilever resonance. Using photothermal excitation results in clean contact, resonance spectra that closely match the ideal frequency response of the cantilever, allowing unambiguous and simple resonance frequency and quality factor measurements in air and liquids alike. This extends the capabilities of CR-FM to biologically relevant and other soft samples in liquid environments. We demonstrate CR-FM in air and water on both stiff silicon/titanium samples and softer polystyrene-polyethylene-polypropylene polymer samples with the quantitative moduli having very good agreement between expected and measured values. © 2015 AIP Publishing LLC. [http://dx.doi.org/10.1063/1.4928105]

The use of atomic force microscopy (AFM) as a nanoscale material characterization tool has increased in the last two decades due to its versatility in generating contrast from a variety of physical properties, such as electrical, magnetic, morphological, and mechanical properties. While AFM routinely provides contrast, acquiring quantitative measurements is notoriously difficult.[1–7]

This paper focuses on contact resonance force microscopy (CR-FM), a technique based on dynamic contact mode of AFM, and originally developed to measure elastic properties of stiff materials.[8–12] In the CR-FM techniques, vibrational resonances of the AFM cantilever are excited while the tip is in contact with the sample. A notable advantage of CR techniques over static deflection based techniques is a higher sensitivity to contact stiffness as it measures frequency shifts of the cantilever and has better signal-to-noise from resonance amplification. CR techniques are implemented by mechanical excitation of either the sample (atomic force acoustic microscopy, AFAM)[10] or the cantilever base (ultrasonic AFM, UAFM).[11] Recently, CR-FM has been extended to measure viscoelastic properties of materials.[13–15] In this technique, henceforth referred to as viscoelastic CR-FM, the changes in contact resonance frequency and quality factor are tracked and recorded. Using the Euler-Bernoulli cantilever beam model, the frequency and $Q$ values are related to the tip-sample contact stiffness and damping. Contact mechanics are then used to generate maps of storage and loss moduli, as described in detail elsewhere.[16]

To date, CR-FM has rarely been employed in aqueous media, in part due to difficulties associated with obtaining clean contact cantilever transfer functions.[17,18] Furthermore, characterization of CR-FM results obtained in liquid environments requires additional analysis and is currently an active area of research.[19–22] Nonetheless, an important advantage of performing CR-FM imaging in liquid is the elimination of capillary adhesion forces present during air imaging. Additionally, many samples, most notably biological ones, require hydration to preserve their native state for mechanical property measurements.[23,24]

Here, we demonstrate photothermally actuated[25–27] viscoelastic CR-FM in air and water over a wide range of moduli.[28] We compare topography, frequency, Q factor results obtained in air and in water.

Furthermore, we report calculated values of storage modulus, loss modulus, and loss tangent factor for different samples based on an internal calibration approach detailed later in the text. The samples investigated included very stiff materials (~150 GPa)—a silicon wafer with a titanium metal evaporated film and a softer (~3 GPa) ternary polymer blend composed of polypropylene (PP), polyethylene (PE), and polystyrene (PS). All CR-FM experiments were conducted on a Cypher AFM (Asylum Research, Santa Barbara, CA) equipped with a contact resonance sample actuator and a blueDrive™ photothermal excitation module. While imaging in liquid, a droplet cantilever holder was used with 18.2 MΩ water. All cantilevers had a nominal spring constant of 2 N/m (AC240 Cantilevers, Olympus Corporation, Tokyo, Japan coated with a 5 nm layer of Cr and 50 nm of Au) with a free cantilever resonance of approximately 70 kHz and a corresponding first flexural mode contact resonance occurring in a range of 260 to 300 kHz. To allow for a direct comparison between both drive methods, the frequency response of the cantilever in contact with the sample was first measured using the sample actuator, then immediately followed by a measurement performed with photothermal excitation (Figures 1(b) and 1(c)). The resonance frequency was tracked using the dual AC resonance tracking (DART) technique, where the cantilever is maintained at its contact resonance frequency by monitoring the amplitude and phase at two frequencies bracketing the contact resonance.[29,30]

---
a)Author to whom correspondence should be addressed. Electronic mail: Roger.Proksch@oxinst.com.

**86**, 083706-1 © 2015 AIP Publishing LLC

a) Diagram and camera view of a photothermally driven cantilever
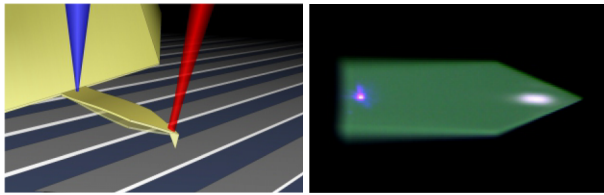


b) Contact tune in air
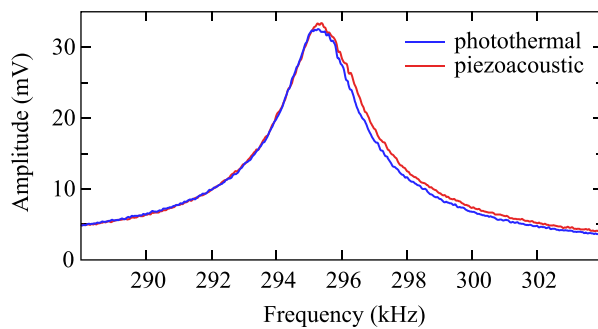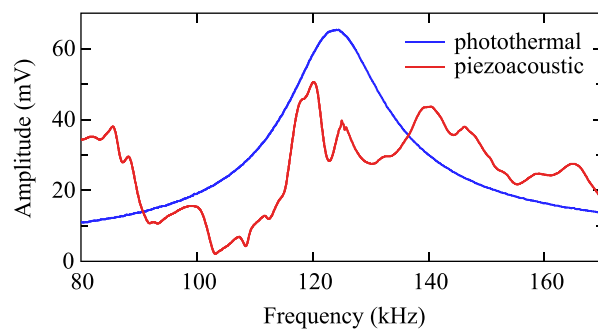


c) Contact tune in water



FIG. 1. (a) Schematic representation of photothermal cantilever excitation during contact resonance imaging. In air (b), contact resonance frequency for piezoacoustic excitation was 295.3 kHz, Q = 138. For photothermal excitation, the contact resonance frequency was 295.4 kHz, Q = 148. In water (c), piezoacoustically actuated spectrum was complex with multiple peaks while the photothermally driven tune showed a single clean peak at 124.1 kHz, Q = 8.1.

To quantify viscoelastic properties, the tip-sample contact is modeled as a driven damped harmonic oscillator, which enables the calculation of the resonance frequency $f$ and quality factor $Q$.[13] The maps of these parameters are then used to obtain viscoelastic material properties as outlined below and discussed in more detail elsewhere.[14,15,31]

A schematic representation of the photothermal cantilever excitation setup is shown in Figure 1(a). As the sample is raster scanned with the cantilever in contact with the surface, cantilever oscillations are induced by modulating the blue laser power that is focused at the base of the cantilever. The fact that no amplitude calibration is required to perform CR-FM is a notable strength of the technique since quantitative amplitude calibration for contact resonance measurements is challenging.[32] The infrared laser that is used to measure the static cantilever deflection is also used to measure the dynamic response of the cantilever driven by photothermal excitation.

Representative contact resonance frequency spectra of a silicon probe on a silicon surface are shown in Figures 1(b) and 1(c), where the piezoacoustic excitation and the photothermal excitation responses are plotted. The results in air for both
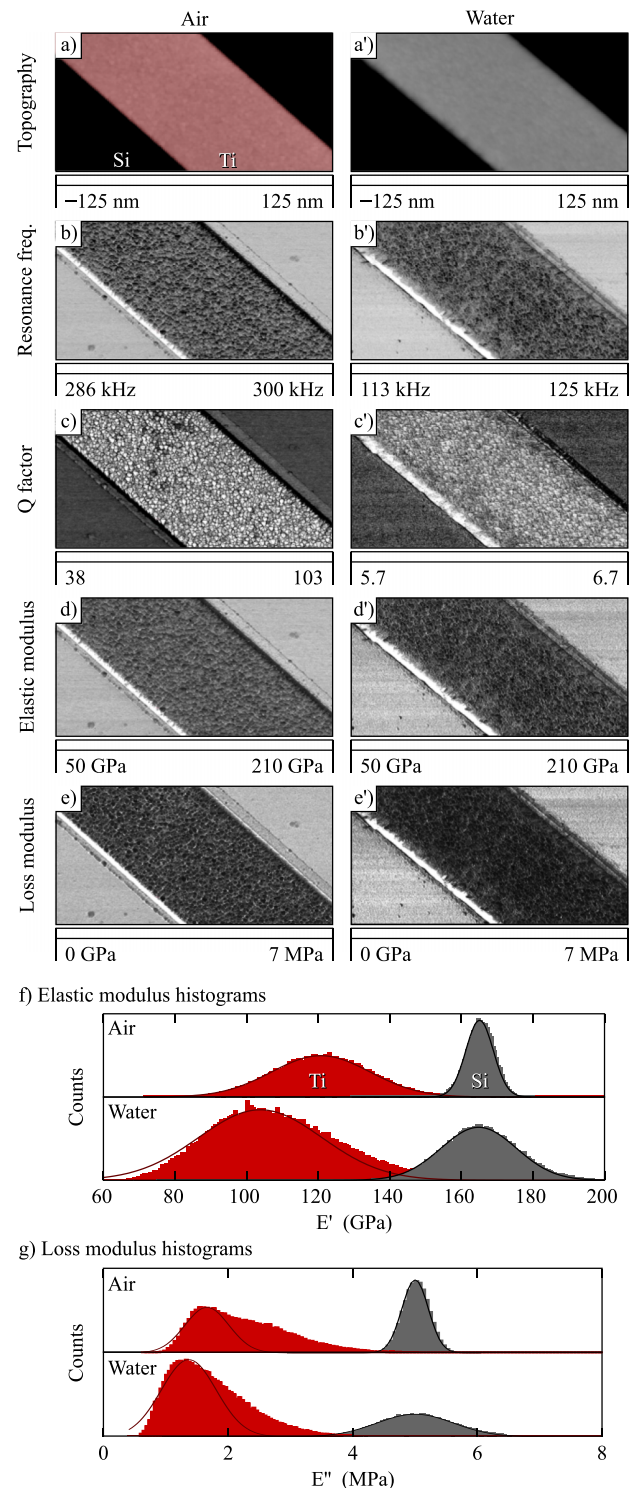


f) Elastic modulus histograms



g) Loss modulus histograms



FIG. 2. Contact resonance images (5 $\mu$m $\times$ 10 $\mu$m) of a titanium film evaporated onto a silicon surface. Results in the left column were acquired in air and results in the right column were acquired in water. (a) and (a′) show the sample's topography, (b) and (b′) show contact resonance frequency of the cantilever, (c) and (c′) show $Q$ factor, (d) and (d′) show the calculated elastic modulus ($E'$), and (e) and (e′) show the calculated loss modulus ($E''$). In (f) and (g) are histograms of the $E'$ and $E''$. The loading forces were ~800 nN in air and ~700 nN in water.

excitation methods are very similar. The advantage of using photothermal excitation becomes clear when the contact resonance tunes are performed in water, as shown in Figure 1(c). In contrast to the clean single contact resonance peak obtained by photothermal excitation, the shape of the contact resonance peak obtained with piezoacoustic excitation is distorted by the "forest of peaks."[17,33–35]

Figure 2 shows a 5 $\mu$m × 10 $\mu$m area of a titanium film evaporated on silicon sample that was first imaged in air and subsequently in water; both images were acquired using photothermal excitation. Topography images (Figures 2(a) and 2(a′)) reveal ~200 nm high, rough titanium stripes on a smooth silicon surface.

The contact resonance frequency (Figure 2(b)) is higher (~290 kHz) on silicon surface in comparison to titanium (~280 kHz), which is consistent with the expected higher silicon stiffness. The frequency contrast remains the same (higher on silicon and lower on titanium) regardless of the imaging environment (air or water).

Images of $Q$ factor values associated with material damping are shown in Figures 2(c) and 2(c′). Values observed on titanium were higher than those on silicon, a result which was unexpected and is still under investigation. A control experiment on a silicon oxide grid with similar geometry and pit depth as the Si-Ti sample confirmed that the height difference between Si and Ti bears no influence on the frequency and $Q$ factor results (see the supplementary material).[38] Other considerations beyond the scope of this work may effectively influence the observed $Q$ factor results. For example high sample roughness (Ti) or low indentation depth on one of the materials may effectively affect the tip-sample interaction and result in unexpected $Q$ values observed on silicon.[21] Furthermore, since the damping on metals and ceramics is low (compared to polymers), it is also possible that the observed Q values are dominated by other variables and do not solely reflect the materials response.

Calculated storage ($E'$) and loss ($E''$) moduli of titanium, in air and water, are shown in Figures 2(d) and 2(e) and 2(d′) and 2(e′). The results presented here were obtained using an internal calibration approach where silicon was chosen as the reference material and the median $E'$ and $E''$ were set to 165 GPa and 5 MPa, respectively.[36] The expected and calculated $E'$ and $E''$ values for all the sample materials are summarized in Table I. Although the $E'$ values of titanium are in the expected range, there is a significant decrease in the titanium modulus when imaged in water. Since the modulus is not expected to change depending on the environment, it is

possible that the results need to be corrected for damping and fluid loading as proposed by Tung *et al.* and Parlak *et al.*[21,22] Such in depth analysis is beyond the scope of this paper and will be considered in future work.

The next sample is a soft "ternary" blended polymer composed of PP, PE, and PS with moduli ranging between 2 and 3 GPa (see Table I).[16] Figure 3(a) shows the topography (in air) of the sample. The topography image acquired in water (Figure 3(a′)) shows improved imaging resolution, presumably due to reduced tip-sample adhesion and lack of capillary forces.

The force applied during imaging varied between 700 and 800 nN on Si-Ti sample and 130-450 nN on the polymer sample. Although the applied force should not influence the elastic modulus, the imaging force should be chosen depending on the thickness and type of the sample to minimize the stress field or effect of contamination layers.[8]

The contact resonance frequency values shown in Figures 3(b) and 3(b′) were highest on PS and lowest on PE, as expected. Figures 3(c) and 3(c′) show the $Q$ factor images. PS inclusions are well distinguished from PE and PP domains; however, the two latter components show very little contrast between each other. Figures 3(d) and 3(d′) and 3(e) and 3(e′) show the calculated $E'$ and $E''$, respectively. Again, an internal standard was used to estimate the moduli values of the two other components of the ternary blend: the matrix material (PP) was set to be the reference standard with $E'$ of 2.5 GPa and $E''$ of 126 MPa.[16] Figure 3(g) compares the histograms of $E'$ values calculated from the images. In both air and water, the three polymer components are clearly differentiated and the storage moduli exhibited the same elasticity trend as reported previously[16] where PE < PP < PS.

In the case of loss modulus ($E''$), the polymer components are better resolved in water than in air. In both environments, PP exhibits the highest loss modulus and follows the values reported previously.[16] In air, $E''$ of PS and PE are very close (80.1 *vs* 82.9 MPa for PE and PS, respectively). In water, PS and PE are well distinguished, with PS exhibiting higher $E''$ than PE. Unlike the previously reported results where $E''$ was lowest on PS, we observed a loss modulus trend where PE < PS < PP. Figures 3(f) and 3(f′) show the loss tangent, also referred to as tan delta (tan $\delta$). tan $\delta$ is a convenient way to express the ratio of energy dissipated to energy stored in a material where the values are calculated from $E'$ and $E''$ as

$$\tan \delta = E''/E'.$$

Histograms of tan $\delta$ values for each polymer component are shown in Figure 3(i). In air, the tan $\delta$ values agree well with

TABLE I. Summary of elastic ($E'$) and loss ($E''$) moduli values estimated in this work as well as expected values.[36,37] Si and PP are used as internal reference standards.

| Sample | $E'$ measured in air (GPa) | $E'$ measured in water (GPa) | Expected $E'$ values[a] (GPa) | $E''$ measured in air (MPa) | $E''$ measured in water (MPa) | Expected $E''$ values[a] (MPa) |
|---|---|---|---|---|---|---|
| Si | 165.5 ($\sigma = 4.2$) | 165.7 ($\sigma = 13.3$) | 165 | 5.0 ($\sigma = 0.2$) | 5.0 ($\sigma = 0.7$) | 5.0 |
| Ti | 121.5 ($\sigma = 14.3$) | 106.5 ($\sigma = 17.1$) | 110-125 | 1.6 ($\sigma = 0.4$) | 1.3 ($\sigma = 0.5$) | 10 |
| PE red | 2.06 ($\sigma = 0.02$) | 2.08 ($\sigma = 0.12$) | 2.12 | 80.1 ($\sigma = 11.2$) | 79.4 ($\sigma = 8.7$) | 90.6 |
| PP gray | 2.50 ($\sigma = 0.13$) | 2.50 ($\sigma = 0.12$) | 2.50 | 125.2 ($\sigma = 11.8$) | 126.1 ($\sigma = 0.1$) | 126 |
| PS blue | 2.75 ($\sigma = 0.16$) | 2.81 ($\sigma = 0.10$) | 2.84 | 82.9 ($\sigma = 8.0$) | 110.8 ($\sigma = 8.9$) | 52.5 |

[a]Expected values are from time-temperature superposed macroscopic bulk dynamic mechanical analysis (DMA) measurements.[16]
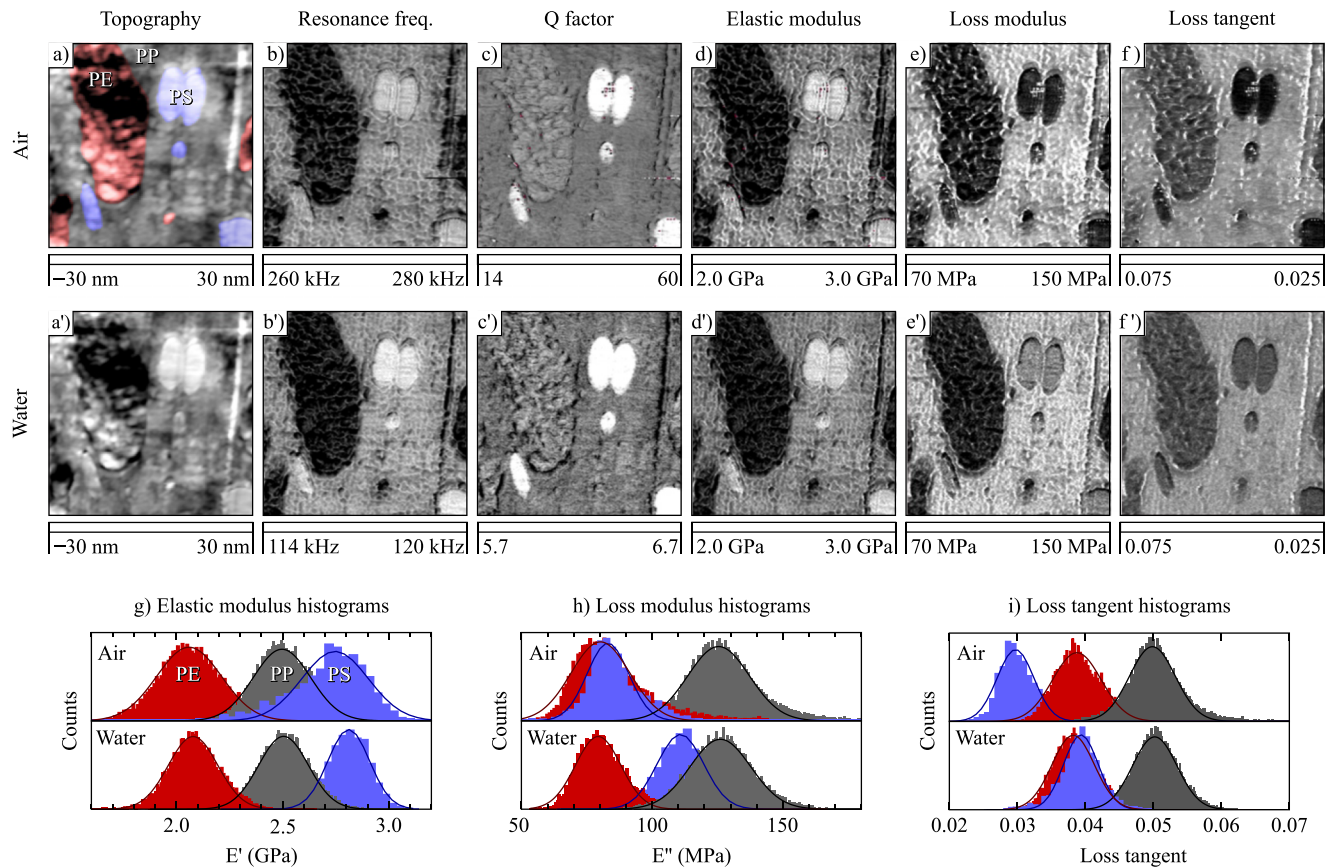
FIG. 3. Contact resonance images (8 $\mu$m × 8 $\mu$m) of a ternary polymer blend composed of polyethylene (PE—red tint), polypropylene (PP—matrix), and polystyrene (PS—blue tint). Results in the top row were acquired in air and results in the lower row were acquired in water. (a) and (a′) show the topography of the sample, (b) and (b′) show contact resonance frequency of the cantilever, (c) and (c′) show $Q$ factor images, (d) and (d′) show the calculated elastic modulus ($E′$) images, and (e) and (e′) show the calculated loss modulus ($E″$) images. Images (f) and (f′) show calculated loss tangent images. In (g) and (h) are histograms of the $E′$ and $E″$. In (i) are histograms of the loss tangent values from the images. Histograms were normalized for simplicity. The loading forces were ~450 nN in air and ~130 nN in water with the cantilever in air and water, respectively.

time-temperature superposed bulk dynamic mechanical analysis (DMA) values.[39] However, in both air and water, the tan $\delta$ values are higher in comparison to DMA values. Plastic deformation of the materials may be a possible explanation for these results.[40] The calculated and expected values of tan $\delta$ are compiled in Table II.

In summary, the aim of this work is to report the first results of photothermal excitation used in liquid to perform contact resonance imaging. We have successfully demonstrated the efficacy of the method by comparing results obtained in air and water on the same location of each sample. Both stiff (silicon/titanium) and softer materials (polymer blend) were successfully imaged in water using photothermal CR-FM. Strong contrast was observed in the frequency data when

imaged in water, even for very similar materials (PS *vs* PP). Although we report storage and loss modulus values in both air and water, correction factors according to the work of Parlak *et al.* as well as Tung *et al.* could be considered for analysis of the results obtained in liquid.[21,22] Loss tangent values were also calculated from the results. In the future, quantitative CR-FM maps of biological tissues may prove valuable for cells, proteins, and biomaterial engineering of materials, such as implants, that are primarily used in liquid environments.

TABLE II. Summary of loss tangent values calculated from E″ and E′ values.

| Sample | Loss tangent in air | Loss tangent in water | Expected values from DMA[a] |
|---|---|---|---|
| PE | 0.039 ($\sigma = 0.004$) | 0.038 ($\sigma = 0.003$) | 0.03 |
| PP[b] | 0.050 ($\sigma = 0.003$) | 0.050 ($\sigma = 0.003$) | 0.05 |
| PS | 0.030 ($\sigma = 0.003$) | 0.039 ($\sigma = 0.003$) | 0.011 |

[a]DMA values are from macroscopic bulk measurements.[16,37]
[b]PP was used as internal reference.

[1]C. J. Gómez and R. Garcia, Ultramicroscopy **110**, 626 (2010).
[2]N. F. Martínez and R. García, Nanotechnology **17**, S167 (2006).
[3]M. Radmacher, R. W. Tillmann, and H. E. Gaub, Biophys. J. **64**, 735 (1993).
[4]A. Rosa-Zeiser, E. Weilandt, S. Hild, and O. Marti, Meas. Sci. Technol. **8**, 1333 (1997).
[5]M. E. Dokukin and I. Sokolov, Langmuir **28**, 16060 (2012).
[6]D. Platz, E. A. Tholén, D. Pesen, and D. B. Haviland, Appl. Phys. Lett. **92**, 153106 (2008).
[7]D. Wang, S. Fujinami, K. Nakajima, and T. Nishi, Macromolecules **43**, 3169 (2010).
[8]D. C. Hurley, "Contact resonance force microscopy techniques for nanomechanical measurements," in *Applied Scanning Probe Methods* (Springer-Verlag, Berlin, 2009), Vol. XI.

[9] D. C. Hurley, K. Shen, N. M. Jennett, and J. A. Turner, J. Appl. Phys. **94**, 2347 (2003).

[10] U. Rabe and W. Arnold, Appl. Phys. Lett. **64**, 1493 (1994).

[11] K. Yamanaka, H. Ogiso, and O. Kolosov, Appl. Phys. Lett. **64**, 178 (1994).

[12] Y. J. Li, N. Kobayashi, H. Nomura, Y. Naitoh, M. Kageshima, and Y. Sugawara, Jpn. J. Appl. Phys., Part 1 **47**, 6121 (2008).

[13] A. Gannepalli, D. G. Yablon, A. H. Tsou, and R. Proksch, Nanotechnology **22**, 355705 (2011).

[14] J. P. Killgore, D. G. Yablon, A. H. Tsou, A. Gannepalli, P. A. Yuya, J. A. Turner, R. Proksch, and D. C. Hurley, Langmuir **27**, 13983 (2011).

[15] P. A. Yuya, D. C. Hurley, and J. A. Turner, J. Appl. Phys. **104**, 74916 (2008).

[16] D. G. Yablon, A. Gannepalli, R. Proksch, J. Killgore, D. C. Hurley, J. Grabowski, and A. H. Tsou, Macromolecules **45**, 4363 (2012).

[17] T. E. Schäffer and P. K. Hansma, J. Appl. Phys. **84**, 4661 (1998).

[18] D. Kiracofe and A. Raman, Nanotechnology **22**, 485502 (2011).

[19] J. E. Sader, J. Appl. Phys. **84**, 64 (1998).

[20] N. Ploscariu and R. Szoszkiewicz, Appl. Phys. Lett. **103**, 263702 (2013).

[21] R. C. Tung, J. P. Killgore, and D. C. Hurley, Rev. Sci. Instrum. **84**, 73703 (2013).

[22] Z. Parlak, Q. Tu, and S. Zauscher, Nanotechnology **25**, 445703 (2014).

[23] S. E. Campbell, V. L. Ferguson, and D. C. Hurley, Acta Biomater. **8**, 4389 (2012).

[24] S. Hengsberger, A. Kulik, and P. Zysset, Bone **30**, 178 (2002).

[25] A. Labuda, J. Cleveland, N. Geisse, M. Kocun, B. Ohler, R. Proksch, M. Viani, and D. Walters, Microsc. Anal. **28**, S21 (2014).

[26] D. Ramos, J. Mertens, M. Calleja, and J. Tamayo, Appl. Phys. Lett. **92**, 173108 (2008).

[27] D. Ramos, J. Tamayo, J. Mertens, and M. Calleja, J. Appl. Phys. **99**, 124904 (2006).

[28] A. Labuda, K. Kobayashi, Y. Miyahara, and P. Grütter, Rev. Sci. Instrum. **83**, 053703 (2012).

[29] B. J. Rodriguez, C. Callahan, S. V. Kalinin, and R. Proksch, Nanotechnology **18**, 475504 (2007).

[30] R. B. Proksch, U. S. patent 20130340126 A1 (19 December 2013).

[31] P. A. Yuya, D. C. Hurley, and J. A. Turner, J. Appl. Phys. **109**, 113528 (2011).

[32] A. Labuda and R. Proksch, Appl. Phys. Lett. **106**, 253103 (2015).

[33] A. Labuda, K. Kobayashi, D. Kiracofe, K. Suzuki, P. H. Grütter, and H. Yamada, AIP Adv. **1**, 022136 (2011).

[34] R. Proksch and S. V. Kalinin, Nanotechnology **21**, 455705 (2010).

[35] T. E. Schäffer, J. P. Cleveland, F. Ohnesorge, D. A. Walters, and P. K. Hansma, J. Appl. Phys. **80**, 3622 (1996).

[36] M. F. Ashby, Acta Metall. **37**, 1273 (1989).

[37] *Materials Properties Handbook Titanium Alloys*, edited by R. Boyer, G. Welsch, and E. W. Collings (ASM International Materials Park, 1994).

[38] See supplementary material at http://dx.doi.org/10.1063/1.4928105 for Figure S1 showing silicon oxide grid image.

[39] D. G. Yablon, J. Grabowski, and I. Chakraborty, Meas. Sci. Technol. **25**, 055402 (2014).

[40] R. Proksch, "Practical considerations for loss tangent imaging with amplitude-modulated atomic force microscopy" (unpublished).